INTERNATIONAL JOURNAL OF MARITIME TECHNOLOGY
IJMT Vol.13/ Winter 2020 (11-19)

Available online at: www. ijmt.ir

Inclination angle effect on ventilation pattern and trailing wake formation of the partially submerged propeller

Ehsan Yari [1*], Ali Barati Moghaddam[2]

[1] *Assistant professor, Department of mechanical engineering, Maleke-Ashtar University of Technology; ehsanyari11@gmail.com*

[2] *Msc Student, Maleke-Ashtar University of Technology, ali.barati.moghaddam@gmail.com*

ARTICLE INFO

Article History:
Received: 05 Oct. 2019
Accepted: 09 Feb. 2020

Keywords:
Partially submerged propeller
Ventilation pattern
Wake formation
Inclination angle

ABSTRACT

Partially submerged propellers function in two-phase condition, i.e. each propeller blade enters water once in each revolution so the thrust and torque of each blade hit maximum level and then become around zero. Surface-piercing propeller investigated in this work is a new geometry that the main purpose of its design has been to achieve higher hydrodynamic performance; minimizing energy loss by reducing of the volume fraction of the water adhered to the exiting blade from the water surface. In this article, Reynolds-Averaged Navier–Stokes computations based on finite volume method (FVM) was applied to investigate force excitation, ventilation pattern and wake formation of the partially submerged propeller under inclination angle. Two-phase flow field equations were solved using homogenous Eulerian multiphase model by sliding method. To solve two-phase flow field at the free surface accurately and deal with free surface effects in calculations, CFX free surface model based on volume of fluid (VOF) approach was used. The accuracy of the numerical method was verified using series of simulations on SPP-841B propeller with existing experimental measurements. Comparison between simulated and measured SPP-841B open characteristics as well as ventilation pattern of the key blade indicated a reasonable agreement with experimental data and observations. Based on obtained data, with an increase in shaft inclination angle, propeller thrust and torque coefficients increased, whereas the propeller efficiency was decreased.

1. Introduction

Nowadays, given the high demand for surface-piercing propellers in a wide range of vessels, many scientists are working on numerical and experimental studies of these propellers. Schematic diagram of the three major flow regimes (for 2D cross section of surface piercing propeller) is shown in Figure1 from water entry until it comes out from water.

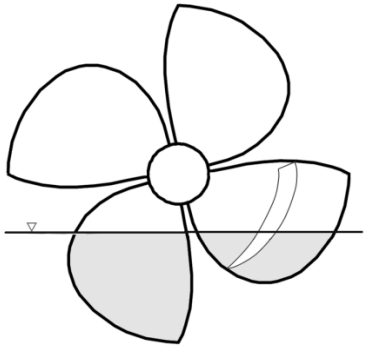

a) Four bladed partially submerged propeller

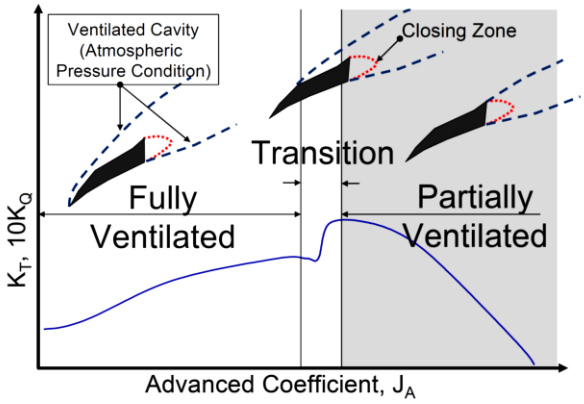

b) Various regimes of ventilation pattern

Figure 1. Partially submerged propeller schematic and fluid flow pattern

The majority studies on the surface-piercing propellers in the past were based on experimental tests. Among these studies, some researchers extracted time-averaged thrust, torque, bending moments and lateral forces on specified types of surface-piercing propellers.

However, there were experimental studies in which scholars not only successfully calculated the accurate force and torque on surface-piercing propellers [1,2]. From 1995 onwards, the experimental studies were focused on the effects of different parameters of surface-piercing propellers such as blade profile, shaft inclination angle, and propeller immersion depth [3-6]. Additionally, due to the phenomena like propeller blade vibrations, there are special issues in scaling process. By development of powerful and reliable computational tools, new and interesting avenue has been opened for researchers to carry out numerical studies on surface-piercing propellers.

Since the surface-piercing propellers function in two-phase mode, some phenomena like ventilation, blade vibrations effects, changes in free-surface elevation due to blade entry and exit have to be taken into account in order to achieve accurate and reliable results. Hence, researchers have always faced several challenges in numerical investigation of these propellers. In continue a brief literature review on numerical research is mentioned on surface-piercing propellers. Young and Kinnas developed a 3D boundary element method, designed previously for cavitation analysis, on conventional propellers, to investigate unsteady flow around surface-piercing propellers. Compared with the experimental data, the predicted results were acceptably accurate [7]. To analyze a four-blade surface-piercing propeller, URNAS method was employed by Caponnetto [8]. He used sliding mesh technique to simulate rotational motion of the propeller and surface capturing method to determine water-air interface.

Ghasemi determined the hydrodynamic specifications of at three blade surface-piercing propeller and a six-blade surface-piercing propeller using boundary element method and experimental tests. A critical advance ratio was obtained at transition mode using an empirical equation based on Weber number and pitch ratio [9]. Unsteady RANS method was applied by Himei to study a surface-piercing propeller in open water condition [10]. Yari and Ghassemi [11-14] and Yari [15] applied boundary element and finite volume methods to conduct several studies on surface-piercing propeller for studying the pressure distribution, spraying and water adhesion. These research works included the development of a computational method based on BEM and FVM to predict the partially submerged propeller performance, with and without cup effect.

Alimardzadeh et al. [16] used unsteady RANS method to analyze the surface-piercing propeller introduced by Olfosson at different submerge ratios. Yang et al. [17] used CFD to investigate the influence of artificial ventilation on the hydrodynamic performance of surface piercing propellers under full immersion conditions. The results showed that with the increase of the advance velocity, the efficiency of the propeller with artificial ventilation increased significantly and was greater than that of without-ventilation case.

In this paper, Reynolds-Averaged Navier–Stokes (RANS) computations based on a finite volume method (FVM) was applied to investigate unsteady flow around a special surface-pricing propeller in shaft inclination angle. The propeller operates in immersion ratio of $I=h/D=$ 0.3. ANSYS CFX commercial code was applied to carry out all simulations using CFX sliding mesh technique. Two-phase flow field equations were solved using homogenous Eulerian multiphase model. To solve two-phase flow field at the free surface accurately and deal with free surface effects in calculations, VOF model was used.

2. Governing Equations

The governing equations for the mathematical description of fluid flow are written in the Eulerian framework. The averaged transport equation for conservation of mass may be written as:

$$\frac{\partial \rho}{\partial t} + \nabla \bullet (\rho \mathbf{u}) = 0 \tag{1}$$

where ρ is the mass density and **u** is the fluid velocity vector.

The averaged momentum equation for fluid is:

$$\frac{\partial(\rho \mathbf{u})}{\partial t} + \nabla \bullet (\rho \mathbf{u}\,\mathbf{u}) = -\nabla p + \nabla \bullet (2\mu \mathbf{S}) + \rho \mathbf{g} - \frac{2}{3}\nabla(\rho k) \tag{2}$$

Where p is the pressure of the gas phase, **g** is the gravitational acceleration, μ is the effective viscosity of the gas, k is the turbulence kinetic energy, and **S** is the symmetric part of the velocity gradient tensor.

The standard $k-\omega$ model in this study is based on the Wilcox $k-\omega$ model.

The standard $k-\omega$ model is an empirical model based on model transport equations for the turbulence kinetic energy (k) and the specific dissipation rate (ω). As the $k-\omega$ model has been modified over the years, production terms have been added to both the k and ω equations, which have improved the accuracy of the model for predicting free shear flows.

2.1 k − ω (SST) Model

The shear-stress transport (SST) $k-\omega$ model was developed to effectively blend the robust and accurate formulation of the $k-\omega$ model in the near-wall region with the free stream independence of the $k-\omega$ model in the far field. The SST $k-\omega$ model has a similar form to the standard $k-\omega$ model:

$$\frac{\partial}{\partial t}(\rho k) + \frac{\partial}{\partial x_i}(\rho k u_i) = \frac{\partial}{\partial x_j}\left(\Gamma_k \frac{\partial k}{\partial x_j}\right) + G_k - Y_k + S_k \tag{3}$$

$$\frac{\partial}{\partial t}(\rho\omega) + \frac{\partial}{\partial x_j}(\rho\omega u_j) = \frac{\partial}{\partial x_j}\left(\Gamma_\omega \frac{\partial \omega}{\partial x_j}\right) + G_\omega - Y_\omega + D_\omega + S_\omega \quad (4)$$

In these equations, the term G_k represents the production of turbulence kinetic energy. G_ω represents the generation of ω. Γ_k and Γ_ω represent the effective diffusivity of k and ω. Y_k and Y_ω represent the dissipation of k and ω due to turbulence. D_ω represents the cross-diffusion term. S_k and S_ω are user-defined source terms [18].

2.2 VOF Model

The VOF model can model two or more immiscible fluids by solving a single set of momentum equations and tracking the volume fraction of each of the fluids throughout the domain. Typical applications include the prediction of jet breakup, the motion of large bubbles in a liquid, and the motion of liquid after a dam break, and the steady or transient tracking of any liquid-gas interface.

The tracking of the interface(s) between the phases is accomplished by the solution of continuity equation for the volume fraction of one (or more) of the phases. For the q^{th} phase, this equation has the following form:

$$\frac{1}{\rho_q}\left[\frac{\partial}{\partial t}(\alpha_q \rho_q) + \nabla\cdot(\alpha_q \rho_q \vec{v}_q) = S_{\alpha_q} + \sum_{p=1}^{n}(\dot{m}_{pq} - \dot{m}_{qp})\right] \quad (5)$$

Where $\dot{m}_{qp}$ is the mass transfer from phase q to phase p and $\dot{m}_{pq}$ is the mass transfer from phase p to phase q. S_{α_q}, is zero, but you can specify a constant or user-defined mass source for each phase.

The volume fraction equation will not be solved for the primary phase; the primary-phase volume fraction will be computed based on the following constraint:

$$\sum_{q=1}^{n} \alpha_q = 1 \quad (6)$$

The volume fraction equation may be solved either through implicit or explicit time discretization [19].

3. Propeller Hydrodynamic Characteristics

Hydrodynamic coefficients of the propeller including advance coefficient (J), thrust coefficient (KT), torque coefficient (KQ) and efficiency (η) are defined as below:

$$J = \frac{V_A}{nD}, K_T = \frac{T}{\rho n^2 D^4}, K_Q = \frac{Q}{\rho n^2 D^5}, \eta = \frac{J}{2\pi}\frac{K_T}{K_Q} \quad (7)$$

Where, V_A is advance velocity, n is rotation rate, Dis propeller diameter and ρ is water density. $\overline{T}$ and $\overline{Q}$ represent time-averaged thrust and torque respectively, in one or some completed cycles.

4. Validation Study

Different situations can be studied for numerical analysis involving the water spraying. In these cases, Mixture or Particle models should be used assuming non-homogeneous flow, which are both time-consuming and numerically difficult. However, the model used in the present study is able to extract the flow pattern around the propeller with high accuracy. Experimental measurements of SPP-841B propeller collected by Olofsson [1], are applied to validate the numerical results obtained in this paper. The experimental and CFD model of this propeller and other data are shown in Figure 2, table1 and table2.

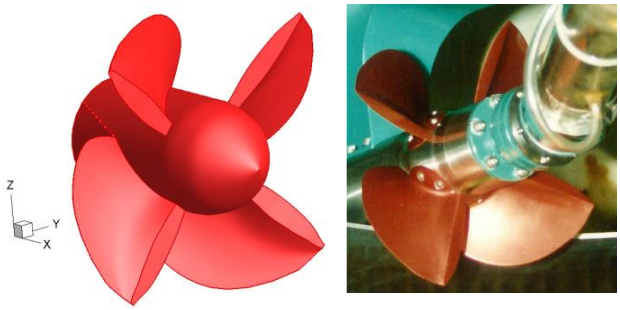

Figure 2. Experimental model of SPP-841B used by Olofsson [1], with corresponding CFD present study model.

Table 1. Main geometric parameters of SPP-841B [1].

Parameter	Symbol	Value
Diameter (mm)	D	250
Hub diameter (mm)	d	85
Pitch at 0.7 radius (mm)	P	310
Hub-diameter ratio	d/D	0.34
Pitch-diameter ratio (r/R= 0.7)	P/D	1.24
Expanded Area ratio	A_E/A_0	0.58
Number of blades	-	4

Table 2. Flow conditions in simulations of SPP-841B, I=h/D=0.33

J	V(m/s)	F_n
1.2	9.39	6

Table 3 shows K_T and K_Q extracted from numerical investigation compare with experimental measurements at J=1.2.

Table 3.K_T and K_Q numerical results compare with experimental measurements at J=1.2 [1].

Parameter	K_T	K_Q
CFD results	0.005685	0.001574
EFD results	0.00553	0.001540
Error (%)	2.80	2.21

Figure 3 demonstrates the comparison between the simulated and measured blade force and moment coefficients of KFx, KFy, KFz, and KMx, KMy, KMz. As shown in this figure, although there are deviations in some regions especially at the blade entry, the simulated values agreed well with the experimental measurements.

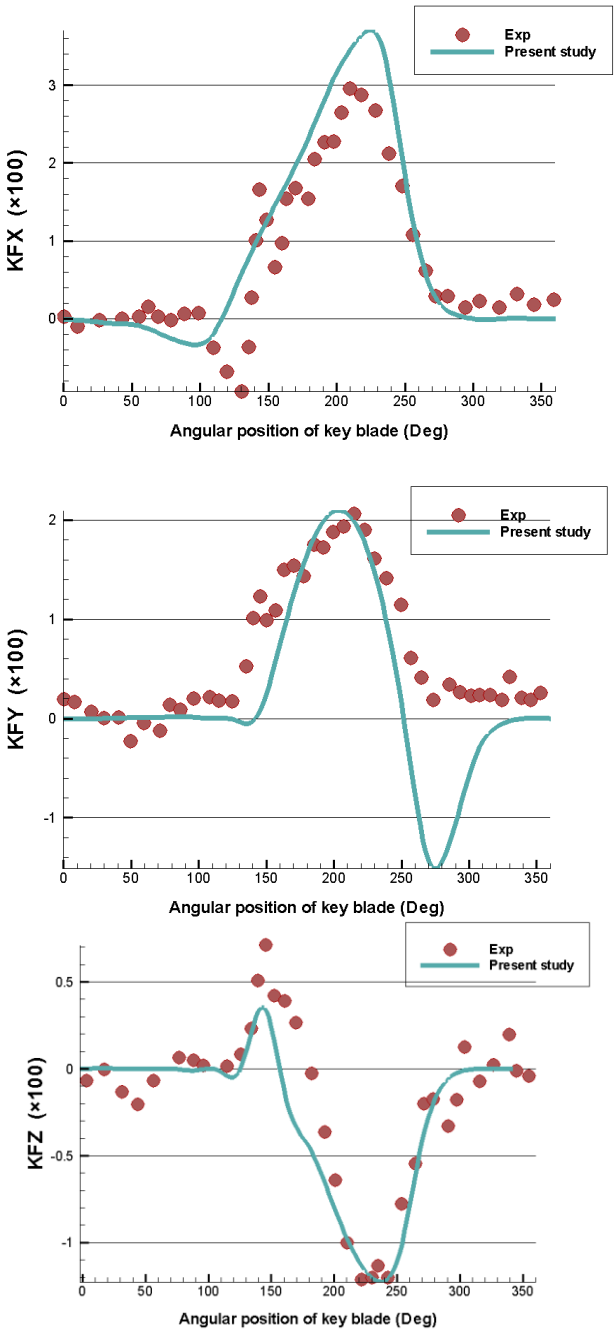

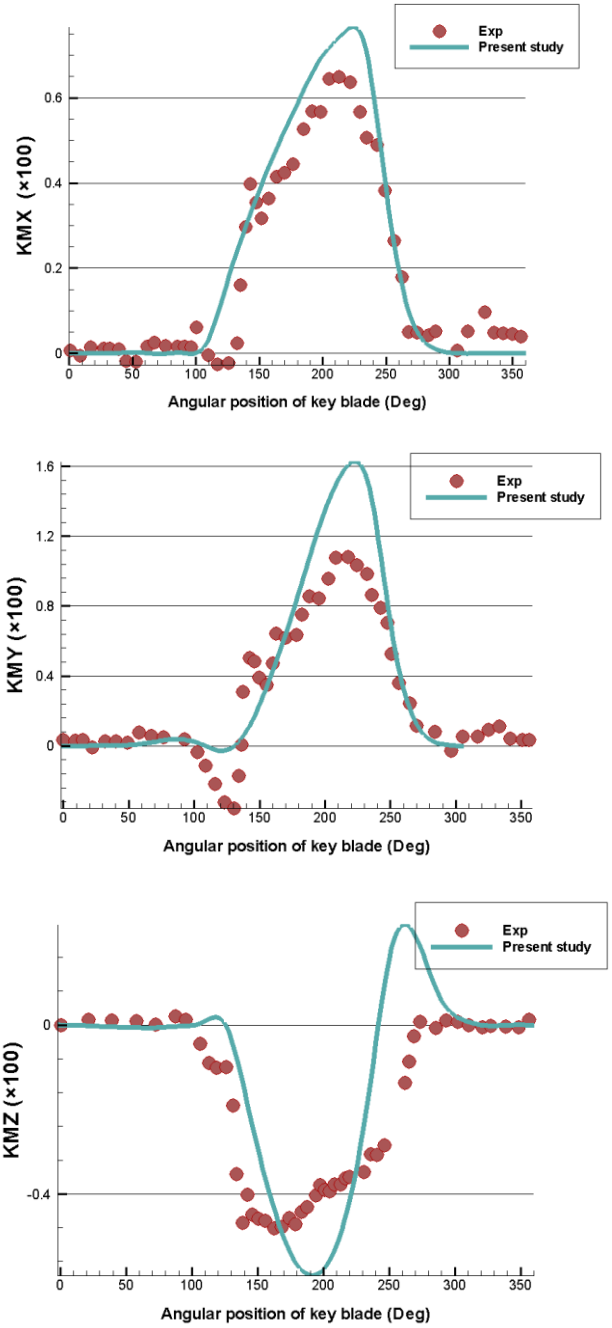

Figure 3. Comparison between the simulated and measured (Exp) [1] force and moment coefficients versus angular position of key blade at J=1.2 for SPP-841B.

5. Results of present study

5.1. Propeller Geometry

The geometric model and main dimensions of the propeller are demonstrated in Figure 4 and Table 4 respectively.

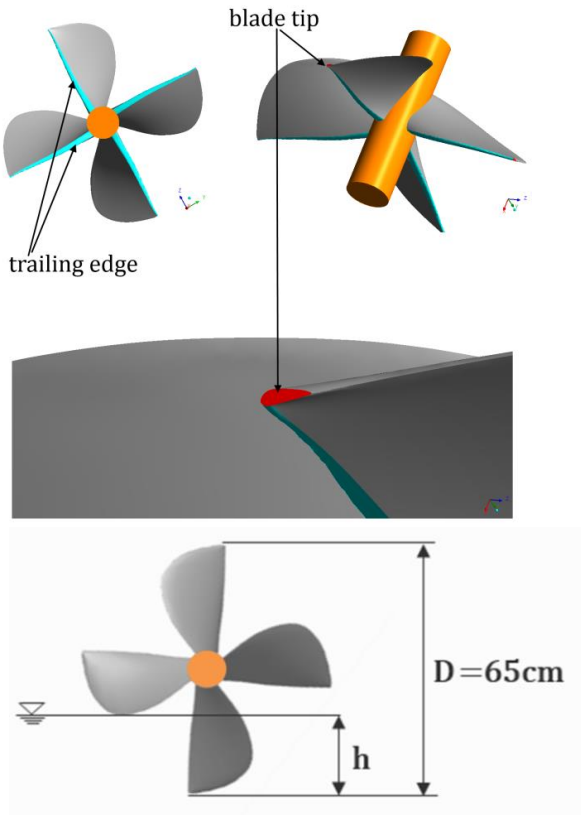

Figure 4. Geometric model of the SPP propeller.

Table4. Main geometric parameters of the Propeller.

Parameter	Value
Diameter (D)	0.65m
Boss ratio (B_r)	0.2
Number of blades (N)	4
Expanded Area Ratio (EAR)	0.45
Section type	Modified

5.2. Computational Domain and Verification

The computational domain is divided into rotating and fixed domains. The former is a cylinder 1.1D in diameter and the latter is a cylinder 7D in diameters. Inlet boundary is located at 2Dupstream and the outlet boundary is placed at 11Ddownstream. Boundary condition for cylindrical side wall was considered to be opening boundary with opening pressure (that use total pressure when the flow direction is into the domain or relative static pressure when it is leaving the domain). Moreover, zero gradient condition was defined for turbulence intensity when the flow direction is into the domain. No slip boundary condition was applied to the propeller.

The motion of rotating domain into the stationary domain was imposed using mesh motion technique With V_A=20 (knot) and n=28 (rps).

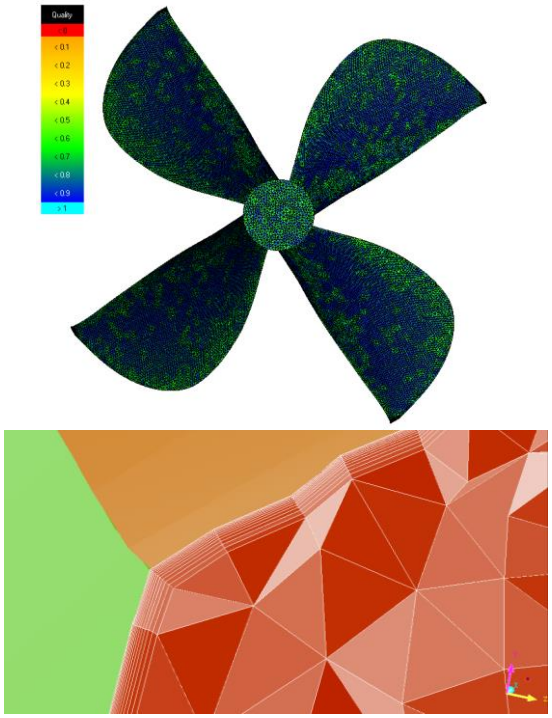

Figure 5. Boundary layer and quality of grid generation over SPP propeller.

In order to perform the grid independence study, five grid configurations were generated using a systematic grid refinement. The variation of thrust coefficient (KT) with the grid size is then investigated. The specifications of the studied grids are shown in Table 3, at J=1.2. It is worth mentioning that for Grid 4, another grid study was conducted. The obtained results showed that refinement in prismatic mesh, using $\Delta y <$ 0.0005m or more than 20 prismatic layers, did not have any significant effect on the resulting thrust coefficient.

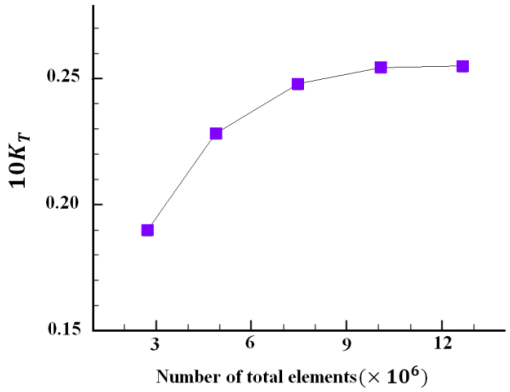

Figure 6. Grid independence study of different mesh distributions at J=1.2.

5.3. Results

Regarding Eq. (7), the predicted hydrodynamic coefficients of the propeller at different shaft inclination angles are indicated in Table 5. According to this table, while thrust and torque coefficients were increased with rise of the shaft inclination angle (ψ), the propeller efficiency (η) was decreased.

Table 5. Predicted hydrodynamic coefficients of the propeller at different shaft inclination angles.

ψ(deg)	K_T	K_Q	η
0	0.040284	0.01265	0.557804
5	0.041277	0.013053	0.553886
10	0.042656	0.013670	0.546555
15	0.044496	0.0145254	0.536565
25	0.046330	0.0161855	0.501129

As the homogenous Eulerian multiphase model is employed in the present study, air and water are regarded as continuous phases in a separated system. Therefore, significant splashing around the blades cannot be simulated. To deal with splashing around the propeller, inhomogeneous multiphase flow model along with Mixture or Particle approaches should be used which are significantly more time consuming and challenging. However, the procedure applied in this study was capable of predicting flow pattern around the propeller clearly. Predicted flow patterns around the propeller in different shaft inclination angles are illustrated in Figure 7 as iso-surfaces with volume fraction 0.5.

As can be seen, with the increase in angle, the length of the wake of the propeller does not change significantly, but the wake diameter increases in downstream. The length of the Wake region usually dissipated after three full propeller rounds.

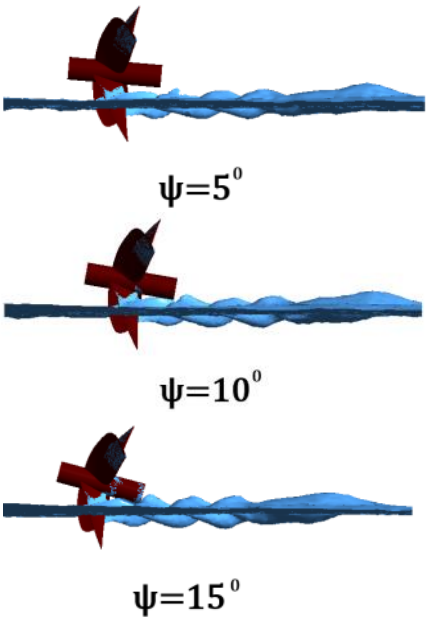

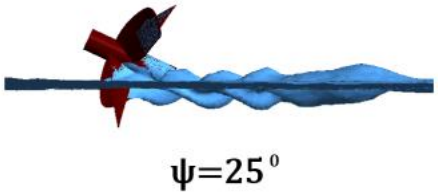

Figure 7. Predicted flow pattern around the propeller in different shaft inclination angles at j = 1.2 and h / D = 0.3

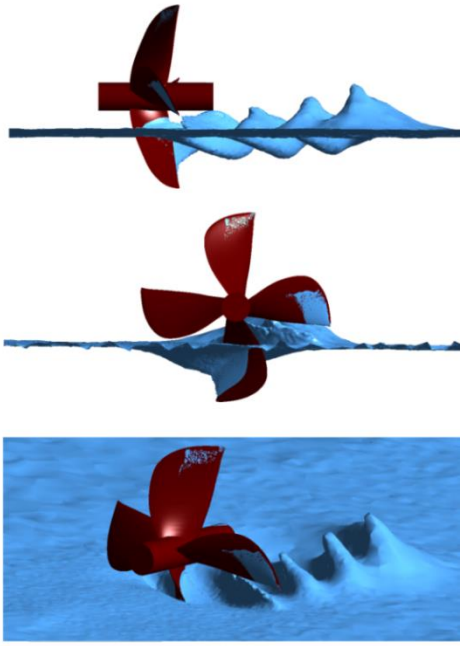

Figure 8. Flow pattern around the semi-submerged impeller at j = 1.1 and h / D = 0.3

According to Figure 8, wake of the propeller is formed in the downstream at below the water surface while in the corresponding position at water surface, free surface rising is observed which these two, does not follow the same trends. In fact, the trailing wake area in the subsurface is largely similar to that of fully submerged propellers, but in the upper part of the water surface, the free surface bulge has sharp peaks that have a different behavior pattern to the subsurface trailing wake.

In addition, the water spray around the blade is visible at the entry and exit from water. The amount of energy loss due to water adhesion at the blade exist is also clearly observed. This rate is greatly reduced by the blade movement in the air, so that no fluid adhesion is observed on re-entry. Very low loss due to adhesion is optimal condition.

Figure 9 shows the volume fraction of the ventilation area over propeller in a one cycle rotation of the propeller. The star mark shows the main blade of the propeller. The ventilation area is shown from the propeller back side. Because in reality the goal is to form and develop the aeration area over behind the blade (propeller back side).

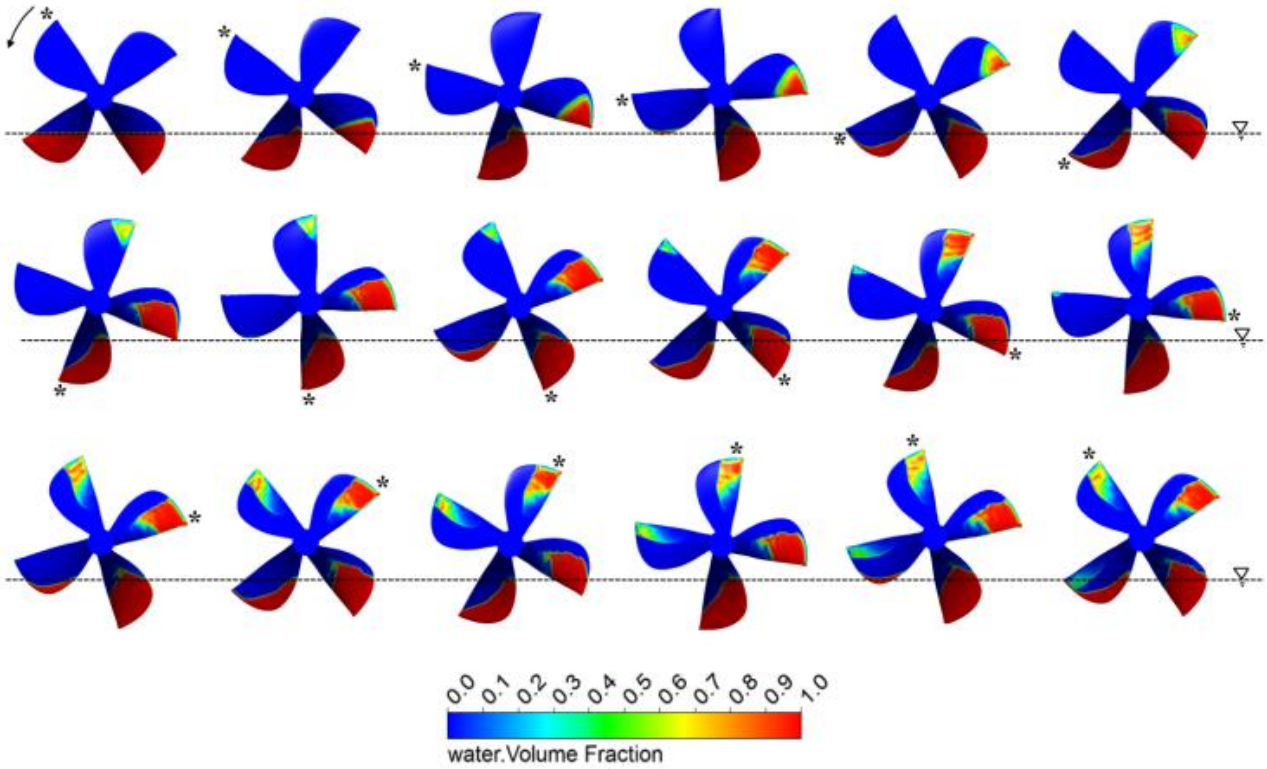

Figure 9. Volume fraction of the ventilation area over propeller.

Fluid volume fraction contours on both sides of the key blade at different shaft inclination angles are shown in Figure 10 for angular position θ=180º. According to the contours, air volume fraction on the pressure side of the blade decreased with an increase in the shaft inclination angle; whereas on the suction side of the blade it remained unchanged from ψ=0º to ψ=15º

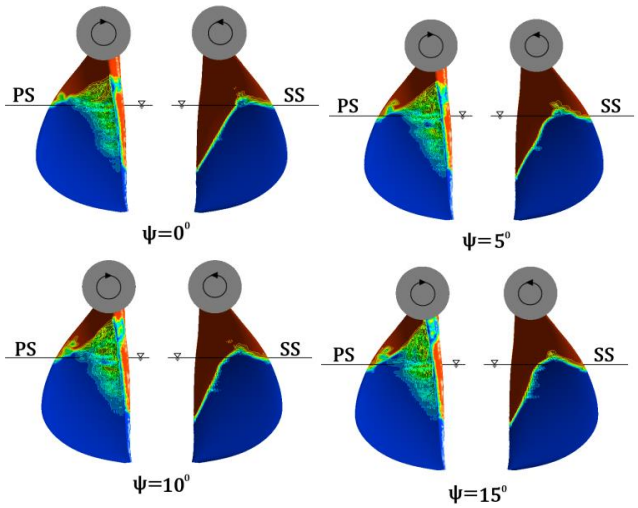

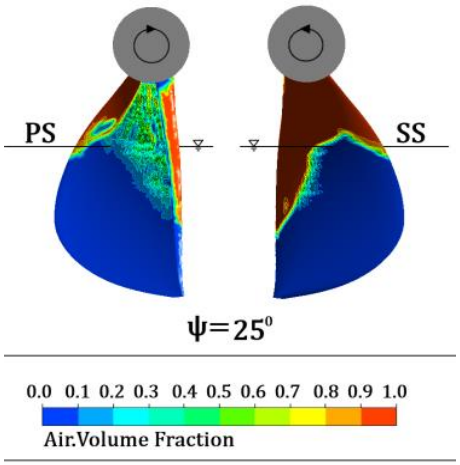

Figure 10. Fluid volume fraction contours on pressure side (PS) and suction side (SS) of the key blade at θ=180º(left), in different shaft inclination angles

In Figure 11, the static pressure distribution over a partially submerged propeller in four different positions during one cycle rotation and at different inclination shaft angles is presented. In all cases with the shaft angle increases, static pressure is increased on the propeller front surface completely noticeable.

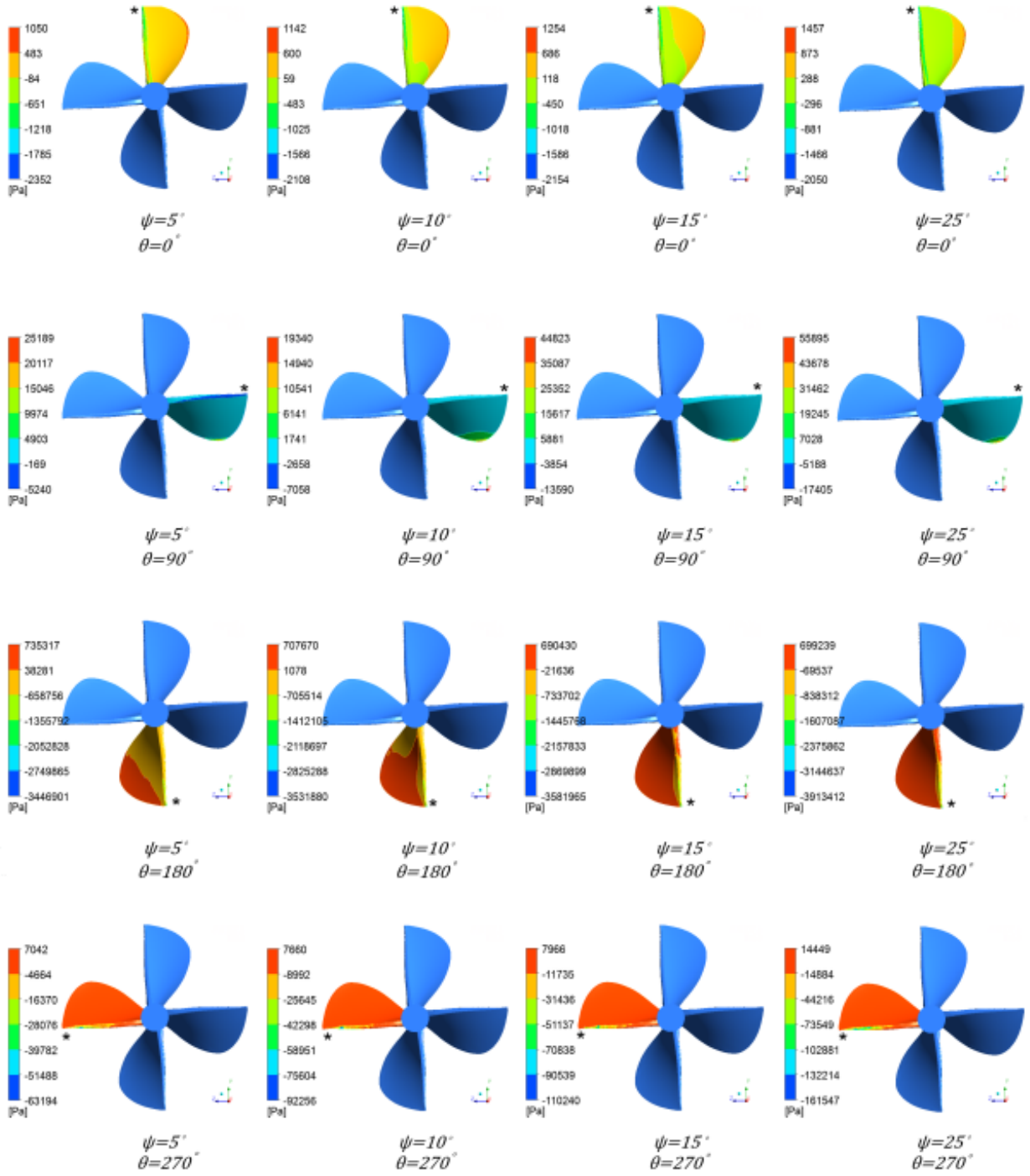

Figure 11. Conture of static pressure at various positions and inclination angle

As shown in Fig. 19, the static pressure occurs at near the trailing edge of the blade in all rotation angles, and also produces a loop with positive pressure difference which brings about a thrust; whereas, there is a negative pressure difference between pressure and suction sides of the section leading to a reduction in total thrust produced by the blade section.

According to cavitation number, operation of the propeller at rotation rate of n=28(rps) can lead to creation of the cavitation but due to operating near the free surface and having access to the atmospheric pressure, cavitation is quickly replaced by ventilation.

6. Conclusions

In this article, CFD based on a finite volume method was used to consider unsteady flow around a partially submerged propeller at immersion one third of diameter. Multiphase VOF model was applied in RANS solver to wake formation and ventilation patterns in range of inclination angle. SPP-841B propeller experimental measurements were applied to accuracy of the numerical method. Comparison between simulated and measured SPP-841B open

characteristics of the key blade indicated a reasonable agreement with experimental data.
Based on obtained results following conclusions were extracted:

- Increasing the shaft angle increases the diameter of the propeller wake.
- The dissipation of the wake begins after three cycle of propeller rotation.
- The water surfaces elevation has a different geometry from corresponding underwater wake and is shaped like sharp peaks.
- As the shaft inclination angle increases, the pressure at the front surface of the blade increases sharply, and therefore the thrust increases significantly.
- The maximum area of the ventilation occurs in the position of 180 degrees of rotation.

7. References

1- N. Olofsson, (1996), *Force and Flow Characteristics of a Partially Submerged Propeller*, Department of Naval Architecture and Ocean Engineering, Chalmers University of Technology, (PhD Thesis).

2- K. Nozawa, N. Takayama, (2002), *Hydrodynamic performance and exciting force of surface piercing propeller*, Proceedings of the Asia Pacific Workshop on Marine Hydrodynamics (APHydro 2002), Kobe, Japan.

3- M. Ferrando, M. Viviani, S. Crotti, P. Cassella, S. Caldarella, (2006), *Influence of Weber number on surface piercing propellers model tests scaling*, Proceedings of the 7th International Conference on Hydrodynamics (ICHD2006), Ischia, Italy.

4- M. Ferrando, A. Scamardella, N. Bose, P. Liu, B. Veitch, (2002), *Performance of family of surface piercing propellers*, Transactions of the Royal Institution for Naval Architects, 144:63-75.

5- K. Nozawa, N. Takayama, (2002), *Experimental study on propulsive performance of surface piercing propeller*, J. Kansai Soc. Nav. Arch. 237: 63-70.

6- K. Himei, S. Yamasaki, M. Yamasaki, T. Kudo, (2005), *A study of practical supercavitating propeller*, the west- Japan society of naval architects.

7- Y.L. Young, S.A. Kinnas, (2003), *Analysis of supercavitating and surface-piercing propeller flows via BEM*, Computational Mech. 32: 269-280.

8- M. Caponnetto, (2003), *RANSE Simulations of Surface Piercing Propellers*, Proceedings of the 6th Numerical Towing Tank Symposium, Roma, Italy.

9- H. Ghassemi, (2009), *Hydrodynamic characteristics of the surface-piercing propellers for the planing craft*, J. Mar. Sci. Appl. 8: 267-274.

10- K. Himei, (2013), *Numerical Analysis of Unsteady Open Water Characteristics of Surface Piercing Propeller*, Proceedings of the 3rd International Symposium on Marine Propulsors smp'13, Launceston, Tasmania, Australia.

11- E. Yari, H. Ghassemi, (2016), *Numerical study of surface tension effect on the hydrodynamic modeling of the partially submerged propeller's blade section*, J. Mech. 32: 653-664.

12- E. Yari, H. Ghassemi, (2016), *Numerical analysis of surface piercing propeller in unsteady conditions and cupped effect on ventilation pattern of blade cross-section*, J. Mar. Sci. Technol. 21: 501-516.

13- E. Yari, H. Ghassemi, (2016), *Hydrodynamic analysis of the surface-piercing propeller in unsteady open water condition using boundary element method*, Int. J. Nav. Archit. Ocean Eng. 8: 22–37.

14- E. Yari, H. Ghassemi, (2016), *The unsteady hydrodynamic characteristics of a partial submerged propeller via a RANS solver*, J.Mar. Eng. Technol.14: 111-123.

15- E. Yari, (2017), *Time Domain Analysis of the Ventilation around the Partial Immersed Propeller Using Sliding Mesh Method*, Int. J.Mari. Technol. 7: 19-27.

16- S. Alimirzazadeh, S. Nardone, R. Zabihzade Roshan, M.S. Seif, (2016), *Unsteady RANS simulation of a surface piercing propeller in oblique flow*. Appl. Ocean Res. 56: 79-91.

17- D. Yang, Z. Ren, Z. Guo, Z. Gao, (2018), *Numerical Analysis on the Hydrodynamic Performance of an Artificially Ventilated Surface-Piercing*, Water. 10: 1499. https:// doi.org/ 10.3390/w10111499

18- D. C.Wilcox, (1998), *Turbulence Modeling for CFD*. DCW Industries, Inc. La Canada, California.

19- F. R. Menter, (2009), *Review of the SST Turbulence Model Experience from an Industrial Perspective*, International Journal of Computational Fluid Dynamics. Volume 23, Issue 4.